Research in Diagnostic and Interventional Imaging 2 (2022) 100011

Contents lists available at ScienceDirect

Research in Diagnostic and Interventional Imaging

journal homepage: https://www.journals.elsevier.com/redii

Original article

MADplots: A methodology for visualizing and characterizing energy-dependent attenuation of tissues in spectral computed tomography

Matthew A. Lewis, PhD[a], Todd C. Soesbe, PhD[a], Xinhui Duan, PhD[a], Liran Goshen, PhD[b], Yoad Yagil, PhD[b], Shlomo Gotman, MSc[b], Robert E. Lenkinski, PhD[a,c,*]

[a] Department of Radiology, University of Texas Southwestern Medical Center, Dallas, TX, USA
[b] Philips Healthcare, Israel
[c] Advanced Imaging Research Center, University of Texas Southwestern Medical Center, Dallas, TX, USA

ARTICLE INFO

Article History:
Received 27 April 2022
Accepted 21 July 2022
Available online 3 August 2022

Keywords:
Tomography, X-ray computed / methods
Radiographic image interpretation
Computer-assisted / methods/
2D-histograms
Retrospective studies

ABSTRACT

Rationale and objectives: A method for visualizing and analyzing the complete information contained in spectral CT scans using two-dimensional histograms (i.e. Material Attenuation Decomposition plots – MADplots) of the water-photoelectric attenuation versus water-scatter attenuation at the cohort (combination of multiple studies across patients), examination, series, slice, and organ/ROI levels is described.

Materials and methods: The appearance of a MADplot with several standard biological materials was predicted using ideal material properties available from NIST and the ICRU to generate a map for this non-spatial data space. Software tools were developed to generate MADplots as new DICOM series that facilitate spectral analysis. Illustrative examples were selected from an IRB-approved, retrospective cohort of Spectral Basis Images (SBIs) scanned using a pre-release, dual-layer detector spectral CT.

Results: By combining all of the voxels for contrast and non-contrast studies, the predicted appearance of the MADplot was confirmed. Locations of several kinds of tissue, the shape of the tissue distributions in normal lung, and the variations in the manner in which organ-specific MADplots change with pathology are demonstrated for the presence of fat in both the liver and pancreas highlighting the potential use for identifying pathologies on spectral CT images.

Conclusions: The examples of MADplots shown at cohort (combined studies), examination, series, slice, organ, and ROI levels illustrate their potential utility in analyzing and displaying spectral CT data. Future studies are directed at developing MADplot based organ segmentation and the automated detection and display of organ based pathologies.

1. Introduction

The potential to generate material selective maps or images based on the energy dependent attenuation of X-ray photons as they pass through tissues predates computed tomography (CT) [1]. A map of the endogenous concentration of iodine in human thyroid was published in 1958 [2] and an image of the distribution of an IV administered iodinated contrast agent in the liver of a rabbit was published in 1959 [3]. Hounsfield's initial paper published in 1973 on CT describes perhaps the earliest approach for distinguishing materials based on their atomic numbers by acquiring images at two different X-ray tube voltages [4]. In 1976, Alvarez and Macovski presented a spectral CT algorithm that extracts the maximum amount of spectral information from two energy-dependent scans [5–7]. This algorithm creates two images through a non-linear transformation from the high and low energy sinograms to a new pair of sinograms containing the projection coefficients in terms of two basis vectors. A number of basis vectors have been described including the use of a basis pair comprised of the photoelectric effect (PE) and Compton scattering (SC), the two dominant tissue interaction mechanisms for diagnostic X-rays [5,7-10]. While an approach using PE and SC as

Abbreviations: CT, computed tomography; DICOM, Digital Imaging and Communications in Medicine; HU, Hounsfield Unit; ICRU, International Commission on Radiation Units and Measurements; IV, intravenous; kVp, peak voltage across an X-ray tube; MADplot, Material Attenuation Decomposition histogram; NIST, National Institute of Standards and Technology; PE, photoelectric; PO, positive oral contrast; ROI, region of interest; SBI, spectral basis images

* Corresponding author at: University of Texas Southwestern Medical Center, Department of Radiology, 5323 Harry Hines Blvd, Dallas, Texas 75390, USA.
E-mail address: Robert.Lenkinski@UTSouthwestern.edu (R.E. Lenkinski).

https://doi.org/10.1016/j.redii.2022.100011

Table 1
Image pairs containing complete spectral CT information on tissue attenuation.

High kVp	Low kVp
Monoenergetic E_1	Monoenergetic E_2
Virtual Non-Contrast (VNC)	Iodine map
Virtual Non-Calcium (VNCa)	Volumetric bone mineral density (vBMD)
Photoelectric	Scatter
Effective Z	Electron density, ρ
Conventional CT	MADplot

basis vectors was one of the earliest described (see for example [5]), it has not been uniformly adopted in the recent emergence of clinical spectral CT. It was suggested by Alvarez [5] that the two-basis model using PE and Compton scattering would need optimization to improve its accuracy.

The advantage of an optimized two basis model is that it minimizes beam hardening artifacts by using optimal base and projection domain decomposition. Another advantage of any PE/SC based decomposition is the strict positivity of the decomposition coefficients, as opposed to decomposition with two specific materials (such as water and iodine) where unphysical, negative densities are routinely encountered and may present a conceptual problem for subsequent tissue characterization. In most spectral CT applications, images created using two basis vectors are further transformed into pairs of quantitative images (with units of effective density in mg/ml or mg/cm^3) using an additional linear transformation, often referred to as a two-material decomposition (2MD). A routine example of this second transformation is the generation of a quantitative iodine map and a virtual non-contrast (VNC) image containing only tissues with iodine removed. As summarized in Table 1, there are numerous potential representations of the information provided by a spectral CT study.

At a minimum, two quantitative values are required per voxel to properly characterize the X-ray attenuation [11], but it has been argued that up to four basis vectors may be appropriate for diagnostic imaging [12]. The approach to optimization and modification of two-base models like the PE and SC model has been recently reviewed in detail by Shapira et al. [13].

It is clear that the radiologist cannot visualize the complete information in a spectral CT study by viewing a single series of images. The complete information is encoded in two series, and the challenge is to integrate this additional information into the clinical workflow. One approach has been to render spectral CT as a color imaging modality, either by using a color map for the effective Z spectral derived image, or by superimposing a color, quantitative iodine map on a greyscale conventional, monoenergetic, or VNC series. In this report, we demonstrate that using a 2D histogram analysis of the water-PE and water-scattering images provides an alternative method for interacting with spectral CT data [14–17]. We have previously reported several applications of MADplots to phantom [14], ex vivo [15], animal [16] and human liver segmentation studies [17]. In this report we provide a more detailed discussion of the approach to generating MADplots and provide examples that illustrate their potential use in clinical studies.

There are several spectral CT systems currently available: dual-source CT, systems employing rapid or slow kVp switching, and systems using dual-layer detectors [18-25,26]. Although all of the examples shown here were acquired on a prototype dual-layer detector system [27–29], the approach can be modified for the analysis of spectral CT data acquired using dual-source scanners or scanners using kVp switching.

2. Materials and methods

Spectral CT is a general term that refers to various forms of computed tomography that utilize two or more energy-dependent data acquisitions to improve the model-based reconstruction of the unknown linear attenuation coefficient inside a system of interest [24]. Early practitioners of CT proposed decomposing the energy-dependent attenuation coefficient into two or more energy dependent basis vectors. For dual-energy CT, in which two acquisitions with differing system weighting functions are collected, this two basis set decomposition can be performed either on the attenuation data (i.e., projection- or sinogram-based decomposition) or on beam-hardened corrected images (i.e., image-space decomposition). The original Alvarez and Macovski decomposition was based on photoelectric (PE) effect and Compton scatter [5] basis vectors,

In this work, nominal SBI decomposition coefficients based on a vendor proprietary and optimized basis functions (Philips Healthcare) were transformed to the related decomposition coefficients for water PE/SC basis functions. We refer to these transformed coefficients as MAD coefficients. Specifically, the basis functions of the MAD coefficients are (1) water-Compton, and (2) water-PE plus water coherent scatter, as listed in the NIST database and ICRU databases [30–32].

This enables other vendors to map any DECT results to the same, literature based, model. Also, analogous representations of the spectral CT data from other vendor solutions could be approximated by transformation using a calibration phantom. Early on, Macovski's group found it useful to view these SBIs as 2D correlation plots [5,6] where the y coordinate is the coefficient of the photoelectric effect and the x coordinate is the coefficient of the attenuation due to Compton scattering. While there is some limited vendor support for making scatterplots of spectral CT data (primarily in associated thin client clinical software), we take the approach of generating Secondary Capture DICOM series that contain 2D histograms of the PE and SC values. For convenience, we refer to these statistical plots as Material Attenuation Decomposition plots or MADplots. If the MADplot is displayed with window level and width of 1, it approximates a scatterplot of the same data. Of course, the histogram or scatterplot could also be formed using any other pair of values in described above.

We simulated the appearance of a MADplot with several standard biological materials using a spectral CT simulator developed in MATLAB (Mathworks, Natick, MA) by our group. The position of the various materials shown in Fig. 1 were obtained from ICRU and NIST databases [30–32]. This Figure illustrates the fact that different materials will appear in different locations within the 2D MADplot space. We normalize the decomposition coefficients relative to water and air so that pure water lies at coordinate (1, 1) and air lies at (0, 0). While some ambiguities are not entirely removed, materials that were previously degenerate or isoattenuating in HU (such as iodine and calcium) can now be easily differentiated.

2.1. Spectral CT image database

We chose illustrative examples of applications of the MADplots from the patients who were enrolled for clinical imaging on a pre-release dual-layer spectral detector CT (i.e., a prototype IQon, Philips Healthcare) between May 2015 and December 2016. All of the patients scanned were referred for a clinically indicated conventional CT. Both single-phase and multi-phase studies were preformed, resulting in 193 non-contrast SBIs and 214 IV contrast-enhanced SBIs. Spectral images (such as mono-energetic and quantitative iodine maps) and associated SBIs for each study were generated on the prototype IQon, anonymized locally, stored as DICOM images on a spectral CT-aware version of IntelliSpace Portal (v6.5, Philips

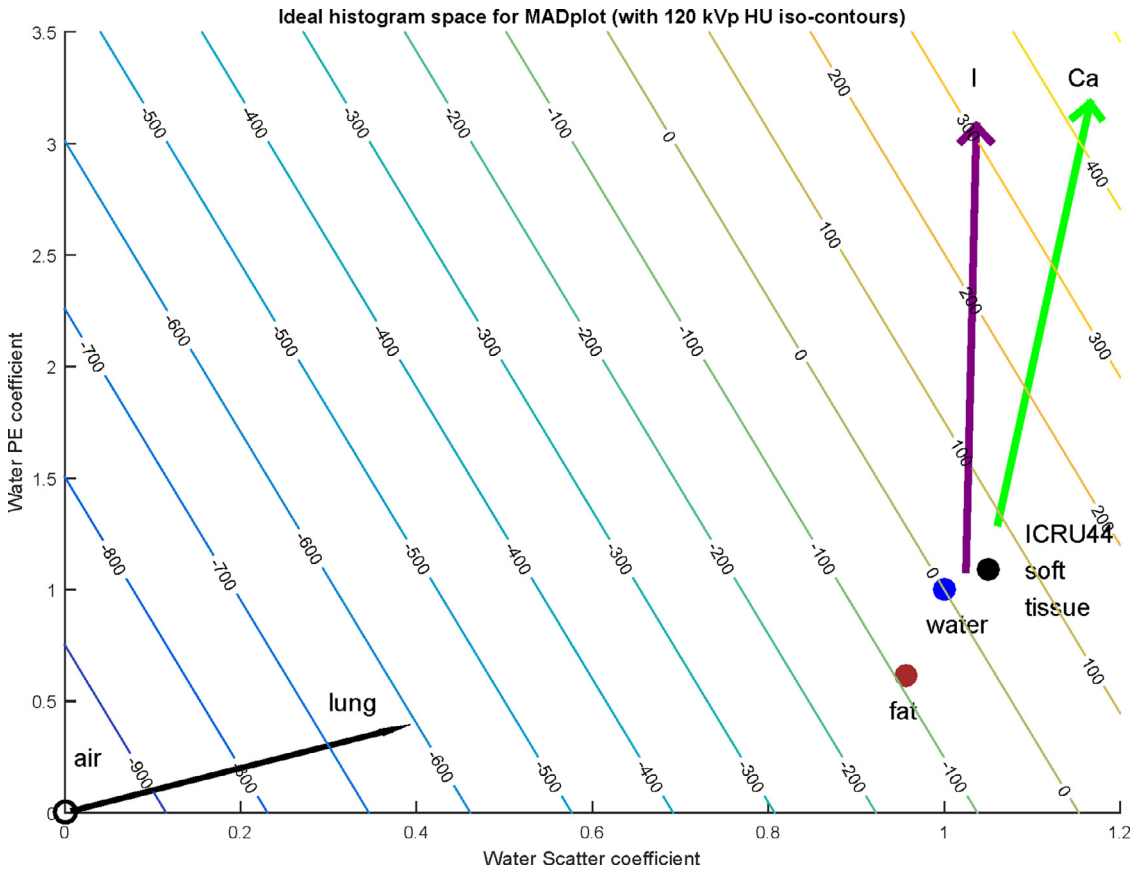

Fig. 1. Nominal locations for various materials [31–33] in the MADplot space. Coefficients for Water PE and Water scatter are relative to those for water at (1, 1). Attenuation iso-contours for conventional polychromatic CT imaging at 120 kVp are shown.. Note: arrows denote axes for typical locations of locations of Calcium (green) and Iodine (purple) with tissue.

Healthcare), and subsequently exported to hard disk for further analysis. In addition, an archival database of just anonymized SBIs was accrued on the departmental research PACS system (iPACS, inVicro, Boston, MA). This database of SBIs was used in generating the examples shown in this report under an IRB approved retrospective review for technical development and image quality assessment.

2.2. MADplot analysis software

We have developed a variety of different software tools that can read the SBIs and create a variety of user selected MADplots. These tools included the popular NIH ImageJ/FIJI software [33] using a modified version of the ScatterJn plugin [34], a 2nd generation tool that used the MATLAB software graphical user interface, and most recently Python-based plugin scripts [35] for the OsiriX family of DICOM viewers.

(OsiriX. www.osirix-viewer.com.; Horos. www.horosproject.org.). These tools provided the capability of creating MADplots from combined CT studies from multiple subjects (Combined MADplots), MADplots of a complete series of the patient's CT examination (Global MADplot), MADplots of a single slice (Local MADplot), and a MADplot of a selected region of interest (ROI MADplot). Each of these tools provided the capability of selecting ROI's on either the corresponding conventional CT image and displaying the locations of the pixels within the ROI on the corresponding MADplot, or conversely, selecting an ROI on the MADplot and displaying the location of the pixels within the ROI on the corresponding convention CT image. In this manner, with the conventional CT and corresponding MADplot displayed side-by-side, the ROI tools allow for the differentiation and visual segmentation of biological materials utilizing their different PE and SC values.

3. Results

Examples of Combined MADplots for all subjects that were scanned without and with IV contrast are shown in Fig. 2. Note that the shapes of these *in vivo* MADplots are very similar to the simulated MADplot shown in Fig. 1. Also note the similarities between Fig.s 2a and b, with the exception of an almost vertical line just to the right of the red arrow seen in Fig. 2b, indicating the presence of iodine. The presence of this line is due to (a) the contribution of the photoelectric effect for iodine increasing the attenuation of X-ray photons and (b) the different concentrations of iodine in various tissues post-injection. This illustrates one of the results of the linear partial volume effect where voxels contain varying homogeneous mixtures of two materials with differing intrinsic attenuations.

An example of a Global MADplot created from the contrast-enhanced scan of a patient is shown in Fig. 3a. ROIs indicated on this MADplot are subsequently demonstrated to corresponded to adipose tissue, intracostal cartilage, and contrast-enhanced liver and spleen (Fig. 3b). Furthermore, this MADplot-based segmentation is compatible with multiplanar reformatting.

At the organ or tissue level, the MADplot representation for pathological versus normal tissue can take various forms. In Figs. 4 and 5,

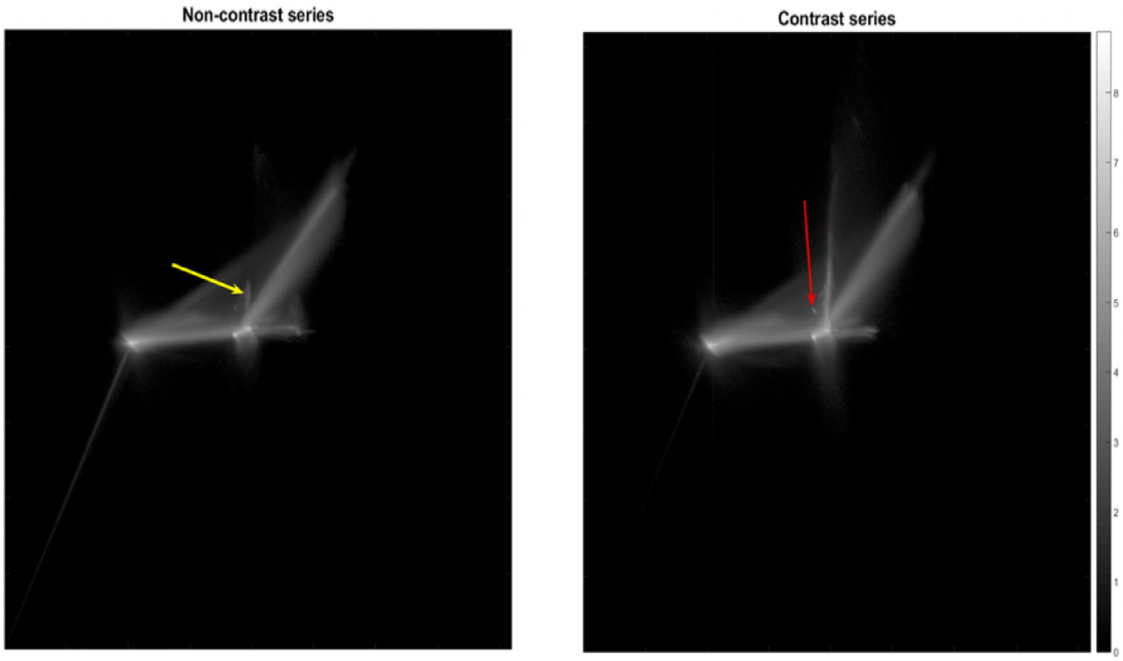

Fig. 2. 2D histograms (i.e. Combined MADplots) for all voxels in Spectral Basis Images from the N=300 studies on the Philips IQon. Histograms are visualized using a base-10 logarithmic scale. Water PE and Water scatter coefficients are given on an arbitrary, relative 12-bit scale. (a) Combined MADplot for all series indicated as non-contrast. The yellow arrow indicates the spectral location of oral contrast not denoted in series descriptions. (b) Combined MADplot for all series labelled as contrast-enhanced. The red arrow denotes a distinct non-biological material: silicone breast implants in 4 subjects.

Fig. 3. (a) A Global MADplot for a male subject with an IV and PO contrast abdomen study. ROIs drawn for locations corresponding to liver with contrast, spleen with contrast, intracostal cartilage, and adipose tissue. (b) Corresponding spatial locations for ROIs in Global MADplot. (c-d) Multiplanar reformating, including spatial ROIs.

we illustrate two possible scenarios for the abnormal presence of fat. As shown in Fig. 4, the homogeneous presence of microscopic fat in the liver can lead to a general translational shift of the MADplot feature that corresponds to liver. This is in contrast to the fatty infiltration and replacement seen in the pancreas in Fig. 5. Here the MADplot representation of the pathological organ is a more complicated change in the distribution of the water-PE and water-scattering values. Changes in the mean and variance are not sufficient in this case to completely characterize the changes in tissue composition, and more sophisticated concepts of statistical distance between non-parametric distributions should be considered.

Lastly an ROI-based MADplot for the lung is shown in Fig. 6. This MADplot shows only the pixels associated with the lung, thus removing any overlap with other organs. The MADplot shows a linear cluster in yellow distributed between the coordinates for air and presumably pure lung tissue, indicating the presence of linear partial volume effects. Since the ROI was generated using thresholding on the interval [-1000,-200] HU, the -200 HU isoattenuation line for the underlying conventional CT is also evident in the ROI-based MADplot.

4. Discussion

2D histograms of spectral data encoded as water photoelectric (plus coherent), and scatter attenuation coefficients (introduced here as MADplots) provide a useful statistically-based method for displaying and analysing spectral CT image information at the series, slice,

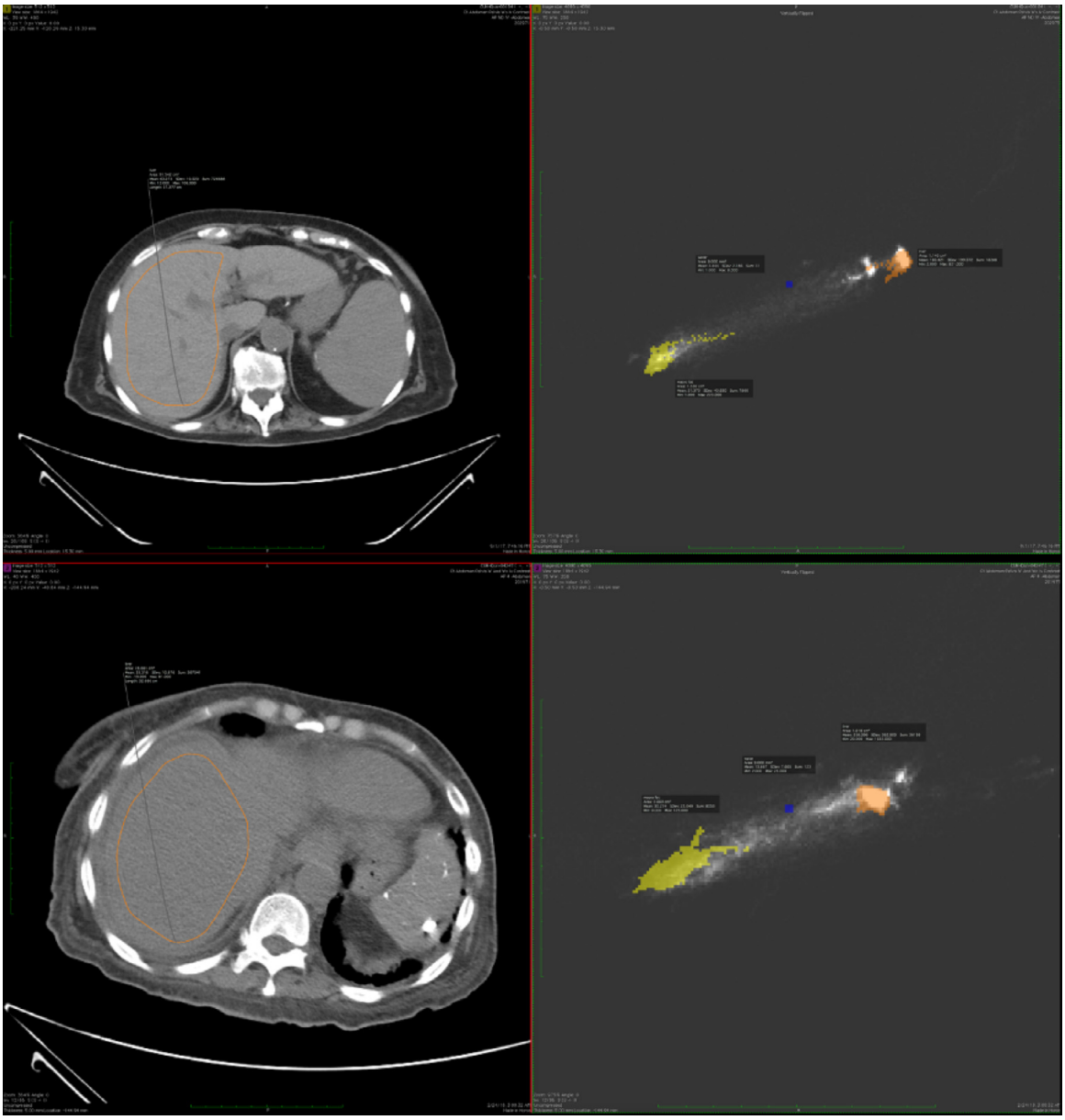

Fig. 4. Local MADplots for non-fatty and fatty liver (zoomed to relevant soft tissue zone). (top) normal liver (mean 63 HU) (bottom) fatty liver (mean 33 HU). Locations of macroscopic fat and water are denoted in MADplot in yellow and blue respectively. Note that liver feature (orange) in MADplot shifts in position with minimal change in shape.

organ, and tissue levels. This particular approach enables setting the relative locations of attenuation coefficients that are predicted for photoelectric absorption and scattering for organs and tissues [36]. The important step in these analyses was the construction of the variety of MADplots as illustrated above. In many cases these MADplots can be calibrated to produce quantitative results that are equivalent to those derived from two material decomposition approaches. Theoretically, these MADplots are independent of the system or tube voltage employed. In our examples, these plots should also be (almost) free of any beam hardening artifacts since they are based on corrected sinograms. The effects of linear partial voluming appear as linear clusters on these MADplots, identifying pixels where there is homogeneous mixing of two materials.

The use of the ROI MADplots could in principle facilitate the development of automated methods for the quantitative analysis of organ specific spectral CT results. One approach to this process could involve the application of an automated organ specific segmentation step, followed by the creation of an ROI MADplot based the segmentation, followed by the creation of a “library” of normal MADplot data and a comparison of the patient data with this normal library to identify any statistically significant differences. These differences could be displayed as an overlay on the conventional CT image for interpretation by the Radiologist.

In quantitative applications of spectral CT, as with quantitative iodine maps, reporting the precision (i.e., the variance) becomes important. Alvarez has provided a detailed analysis of determining

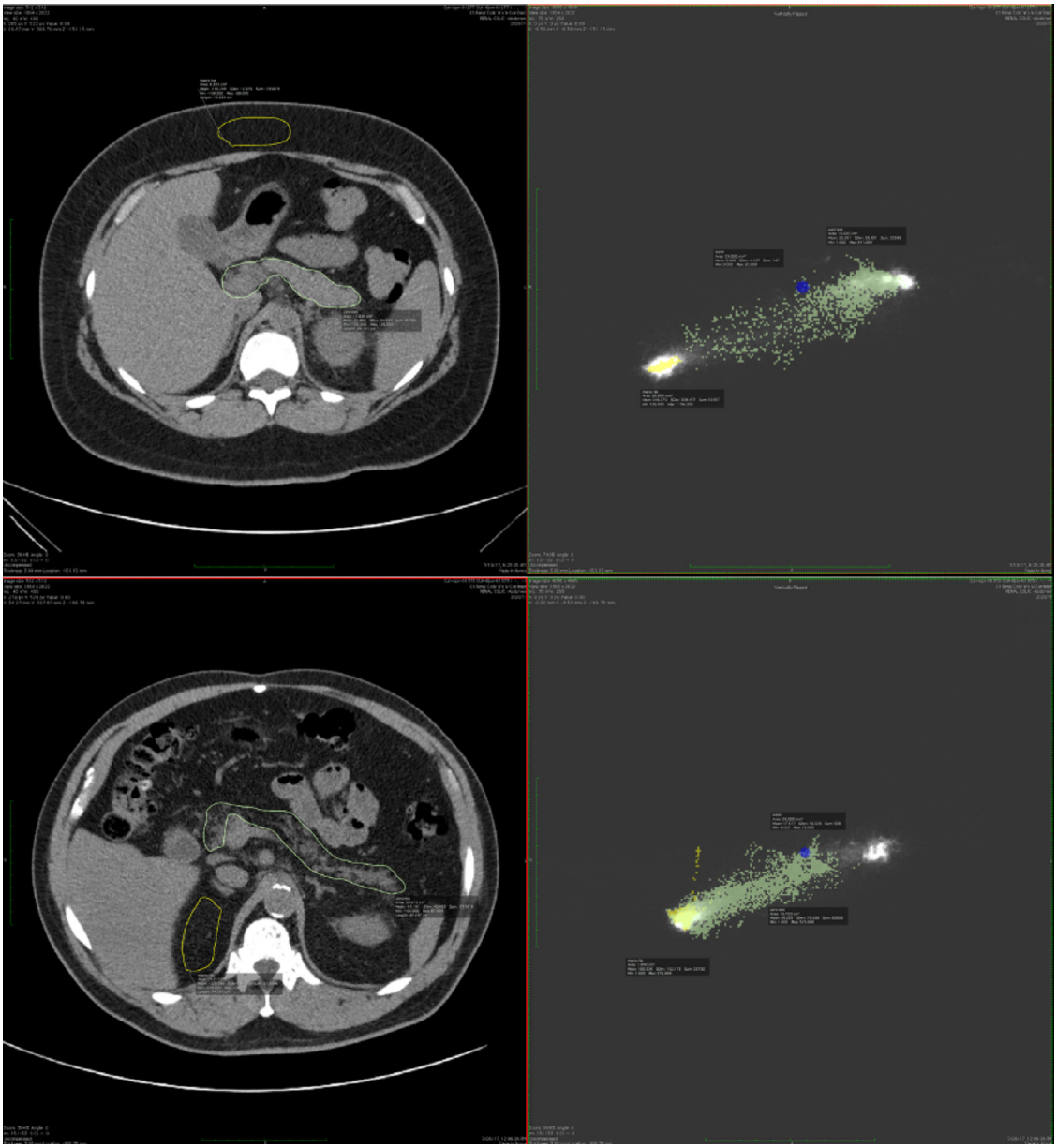

Fig. 5. Local MADplots for normal pancreas and pancreas with fatty infiltration (zoomed to relevant soft tissue zone). (top) normal pancreas. Locations of macroscopic fat and water are denoted in MADplot in yellow and blue respectively. Note that pancreas (green) in MADplot is characterized by a statistical change in the complete distribution of Water PE/ Water scatter values rather an a simple translation.

the variances of the photoelectric effect and Compton scattering [5]. In principle, the variances in the two coefficients can be employed to compute the variance in any quantitative map derived from a MADplot. A limitation of the approach described here is the fact that the accuracy of the MADplots depend in large part on the accuracy of the determination of the two basis vectors from the non-linear transformation applied to the sinograms described above. Any model errors present in this transformation could lead to inaccuracies (or biases) in the MADplots. For example, incomplete scatter correction at the sinogram level could be a source of bias.

At our institution, we have found that the MADplot-centric representation of spectral CT data is viewed more favorably by our radiologist than techniques such as the spectral Hounsfield curve which presents HU mean and variance for an ROI across many monoenergetic keV values [37]. In principle, the spectral Hounsfield curve is highly redundant since it too is linearly related to the underlying two parameter spectral CT data. It is also difficult to imagine a procedure for mapping from spectral Hounsfield curves back to image space, a procedure which is natural in the MADplot representation.

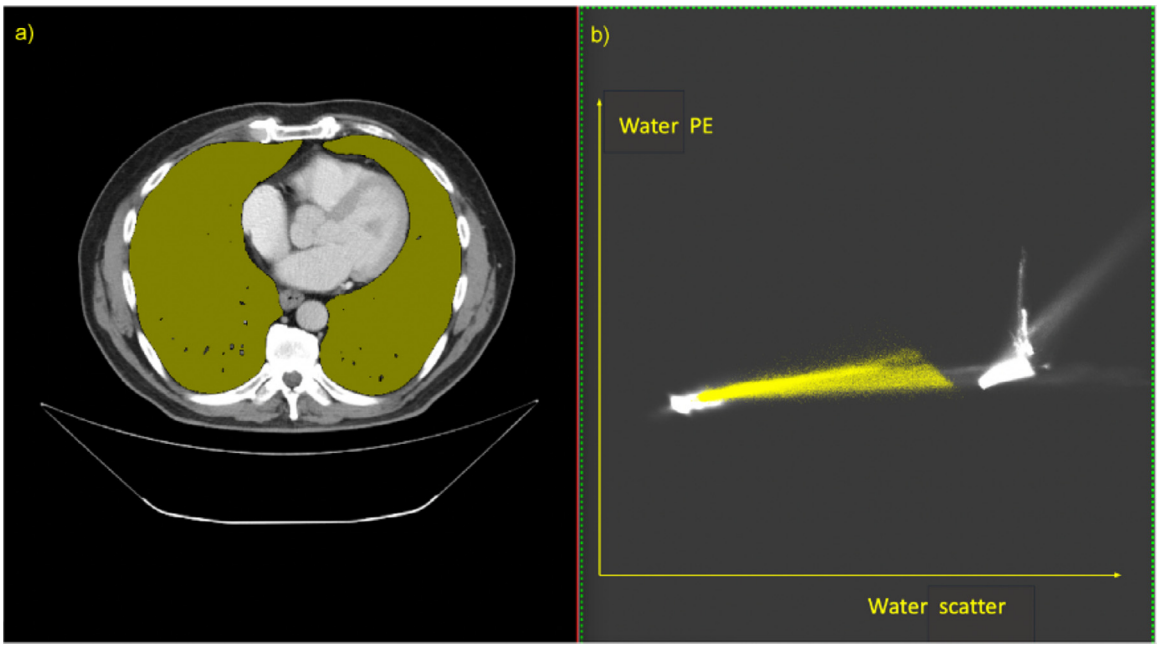

Fig. 6. An example of a ROI-based MADplot for a specific organ (a) ROI of tissue or organ of interest – in this case, bilateral lungs. (b) organ-specific MADplot for lungs (yellow) superimposed on global MADplot for entire chest series. Note: the -200 HU threshold line is evident as a yellow linear boundary in the MADplot.

To our knowledge the MADplot approach for analysis and display of Spectral CT images is not currently available on commercial scanners or their analysis platforms.

5. Conclusions

We have shown examples of MADplots that illustrate some of their potential utility in analyzing and displaying spectral CT data. We suggest that the use of these MADplots may become an important method for identifying pathologies on spectral CT images. Although we have shown examples from a prototype dual-layer scanner, we suggest that this approach can also be applied, after appropriate calibration, to spectral data from scanners based on dual-source or kVp switching. This would potentially provide a framework toward a vendor neutral approach in the clinical interpretation of Spectral CT studies.

Funding

This research was supported by in kind contributions as part of a research grant from Philips Healthcare (Grant No. CRA201809-0011).

Institutional review board statement

The study was conducted according to the guidelines of the FDA and approved by the Institutional Review Board of UT Southwestern Medical Center (protocol code STU-202017 approved on 4/1/2021).

Informed consent statement

Informed consent was waived since this is a retrospective study.

Author contributions

Conceptualization, M.A.L., T.C.B., Y.Y, and REL.; methodology, M.A.L., T.C.S., X.D., Y.Y, S.G., and R.E.L; software, M.A.L, T.C.S., Y.Y., S.G., and R.E.L.; resources, Y.Y., S.G., and R.E.L.; data curation, M.A.L. and T.C.S.; analysis, M.A.L., and T.C.S.; writing—original draft preparation, M.A.L. writing—review and editing, M.A.L., T.C.B. Y.Y., and R.E.L.; supervision, R.E.L.; project administration, M.A.L and R.E.L; All authors have read and agreed to the published version of the manuscript.

Declaration of Competing Interests

None.

References

[1] Lehmann LA, Alvarez RE. Energy-selective radiography a review editors. In: Kereiakes JG, Thomas SR, Orton CG, editors. Digital radiography: selected topics. Boston, MA: Springer US; 1986. p. 145–88.
[2] Jacobson B. Dichromography - method for *in vivo* quantitative nalysis of certain elements. Science 1958;128(3335):1346–8.
[3] Edholm P, Jacobson B. Quantitative determination of iodine *in vivo*. Acta Radiol 1959;52:337–46.
[4] Hounsfield GN. Computerized transverse axial scanning (tomography): part 1. Description of system. Br J Radiol 1973;46(552):1016–22.
[5] Alvarez RE. [Ph.D.]. Stanford University; 1976.
[6] Alvarez RE, Macovski A. Energy-selective reconstructions in X-ray computerized tomography. Phys Med Biol 1976;21(5):733–44.
[7] Macovski A, Alvarez RE, Chan JL, Stonestrom JP, Zatz LM. Energy dependent reconstruction in X-ray computerized tomography. Comput Biol Med 1976;6 (4):325–36.
[8] Avrin DE, Macovski A, Zatz LE. Clinical application of Compton and photo-electric reconstruction in computed tomography: preliminary results. Invest Radiol 1978;13(3):217–22.
[9] Lehmann LA, Alvarez RE, Macovski A, Brody WR, Pelc NJ, Riederer SJ, Hall AL. Generalized image combinations in dual Kvp digital radiography. Med Phys 1981;8 (5):659–67.
[10] Azevedo SG, Martz HE, Aufderheide MB, Brown WD, Champley KM, Kallman JS, Roberson JP, Schnberk D, Seetho IM, Smith JA. System-independent characterization of materials using dual-energy Computed Tomography. IEEE Trans Nucl Sci 2016;63(1):341–50. doi: 10.1109/tns.2016.2514364.
[11] Alvarez RE. Dimensionality and noise in energy selective x-ray imaging. Med Phys 2013;40(11). doi: 10.1118/1.4824057.
[12] Bornefalk H. XCOM intrinsic dimensionality for low-Z elements at diagnostic energies. Med Phys 2012;39(2):654–7. doi: 10.1118/1.3675399.
[13] Shapira N, Yagil Y, Wainer N, Altman A. Spectral imaging technologies and apps and dual-dayer detector solution editors. In: Taguchi K, Blevis I, Iniewski K, editors. Spectral, photon counting computed tomography technology and applications. Boca Raton: CRC Press, Taylor and Francis group; 2020. p. 3–16.
[14] Soesbe TC, Xi Y, Nasr K, Leyendecker JR, Lenkinski RE, Lewis MA. Investigating new CT contrast agents: a phantom study exploring quantification and

differentiation methods for high-Z elements using dual-energy CT. Eur Radiol 2021;31(10):8060–7. doi: 10.1007/s00330-021-07886-x.
[15] Soesbe TC, Lewis MA, Xi Y, Browning T, Ananthakrishnan L, Fielding JR, Lenkinski RE, Leyendecker JR. A technique to identify isoattenuating gallstones with dual-layer spectral CT: an ex vivo phantom study. Radiology 2019;292(2):400–6. doi: 10.1148/radiol.2019190083.
[16] Soesbe TC, Lewis MA, Nasr K, Ananthakrishnan L, Lenkinski RE. Separating high-Z oral contrast from intravascular iodine C contrast in an animal model using dual-layer spectral CT. Acad Radiol 2019;26(9):1237–44. doi: 10.1016/j.acra.2018.09.012.
[17] Ng YS, Xi Y, Qian YX, Ananthakrishnan L, Soesbe TC, Lewis M, Lenkinski R, Fielding JR. Use of spectral detector computed tomography to improve liver segmentation and volumetry. J Comput Assist Tomogr 2020;44(2):197–203. doi: 10.1097/rct.0000000000000987.
[18] Karcaaltincaba M, Aktas A. Dual-energy CT revisited with multidetector CT: review of principles and clinical applications. Diagn Interv Radiol 2011;17 (3):181–94. doi: 10.4261/1305-3825.Dir.3860-10.0.
[19] Schirra CO, Brendel B, Anastasio MA, Roessl E. Spectral CT: a technology primer for contrast agent development. Contrast Media Mol Imaging 2014;9(1):62–70.
[20] Simons D, Kachelriess M, Schlemmer HP. Recent developments of dual-energy CT in oncology. Eur Radiol 2014;24(4):930–9. doi: 10.1007/s00330-013-3087-4.
[21] McCollough CH, Leng S, Yu L, Fletcher JG. Dual- and multi-energy CT: principles, technical approaches, and clinical applications. Radiology 2015;276(3):637–53. doi: 10.1148/radiol.2015142631.
[22] Seidensticker PR, Hofmann LK. Dual source CT imaging. Heidelberg: Springer Medizin Verlag; 2008.
[23] Johnson T, Fink C, Schönberg SO, Reiser MF. Dual energy CT in clinical practice. Berlin, Heidelberg: Springer-Verlag; 2011.
[24] Heismann BJ, Schmidt BT, Flohr T. Spectral computed tomography. Bellingham, WA: SPIE; 2012.
[25] Forghani R, De Man B, Gupta R. Dual-Energy Computed Tomography: physical principles, approaches to scanning, usage, and implementation: part 1. Neuroimaging Clin N Am 2017;27(3):371–84. doi: 10.1016/j.nic.2017.03.002.
[26] Forghani R, De Man B, Gupta R. Dual-energy computed tomography: physical principles, approaches to scanning, usage, and implementation: part 2. Neuroimaging Clin N Am 2017;27(3):385–400. doi: 10.1016/j.nic.2017.03.003.
[27] Carmi R, Naveh G, Altman A. Material separation with dual-layer CT. Nuclear Science Symposium Conference Record. IEEE; 2005. 2005 23-29 Oct. 2005.
[28] Shefer E, Altman A, Behling R, Goshen R, Gregorian L, Roterman Y, Uman I, Wainer N, Yagil Y, Zarchin O. State of the art of CT aetectors and sources: a literature review. Current Radiol Reports 2013;1(1):76–91. doi: 10.1007/s40134-012-0006-4.
[29] Kim SH, Youn H, Kim D, Kim DW, Jeon H, Kim HK. Computed tomography with single-shot dual-energy sandwich detectors. In: Proceedings of the SPIE; 2016.
[30] International Commission on Radiation Units and Measurements (ICRU) ICRU. Report 44, tissue substitutes in radiation dosimetry and measurement. https://www.icru.org/report/tissue-substitutes-in-radiation-dosimetry-and-measurement-report-44/ (ICRU)Date accessed December 2019.
[31] International Commission on Radiation Units and Measurements (ICRU) ICRU. Report 46, photon, electron, proton and neutron interaction data for body tissues. https://www.icru.org/report/photon-electron-proton-and-neutron-interaction-data-for-body-tissues-report-46/ Date accessed December 2019.
[32] National Institue of Standards and Technology (NIST), XCOM: https://physics.nist.gov/PhysRefData/Xcom/html/xcom1.html , Date accessed December 2019.
[33] Schindelin J, Arganda-Carreras I, Frise E, Kaynig V, Longair M, Pietzsch T, Preibisch S, Rueden C, Saafield S, Schmid B, Tinevez JY, White DJ, Hartenstein V, Eliceiri K, Tomancek P, Cardona A. Fiji: an open-source platform for biological-image analysis. Nat Methods 2012;9(7):676–82. doi: 10.1038/nmeth.2019.
[34] Zeitvogel F, Schmid G, Hao L, Ingino P, Obst M. ScatterJ: An ImageJ plugin for the evaluation of analytical microscopy datasets. J Microsc 2016;261(2):148–56. doi: 10.1111/jmi.12187.
[35] Blackledge MD, Collins DJ, Koh DM, Leach MO. Rapid development of image analysis research tools: Bridging the gap between researcher and clinician with pyOsiriX. Comput Biol Med 2016;69:203–12. doi: 10.1016/j.compbiomed.2015.12.002.
[36] Boone JM, Chavez AE. Comparison of x-ray cross sections for diagnostic and therapeutic medical physics. Med Phys 1996;23(12):1997–2005.
[37] Bolus D, Morgan D, Berland L. Effective use of the Hounsfield unit in the age of variable energy CT. Abdominal Radiol 2017;42(3):766–71. doi: 10.1007/s00261-017-1052-4.